J. Fluid Mech. (2026), *vol.* 1032, A52, doi:10.1017/jfm.2026.11361

Quasi-steady aerodynamics predicts the dynamics of flapping locomotion

Olivia Pomerenk[1] and **Leif Ristroph**[1]

[1]Courant Institute of Mathematical Sciences, Applied Math Lab, New York University, New York, NY 10012, USA

Corresponding author: Leif Ristroph, ristroph@cims.nyu.edu

(Received 26 August 2025; revised 5 January 2026; accepted 22 February 2026)

The propulsion of a flapping wing or foil is emblematic of bird flight and fish swimming. Previous studies have identified hallmarks of the propulsive dynamics that have been attributed to unsteady effects such as the formation and shedding of edge vortices and wing–vortex interactions. Here, we show that several key features of heaving flight are captured by a quasi-steady aerodynamic model that aims to predict stroke-averaged forces from wing motions without explicitly solving for the flows. We address the forward dynamics induced by up-and-down heaving motions of a thin plate with a nonlinear model which involves lift and drag forces that vary with speed and attack angle. Simulations reproduce the well-known transition for increasing Reynolds number from a stationary state to a propulsive state, where the latter is characterised by a Strouhal number that is conserved across broad ranges of parameters. Parametric, sensitivity and stability analyses provide physical interpretations for these results and show the importance of accounting for the flow regimes which are demarcated by Reynolds number and angle of attack. These findings extend the phenomena of unsteady locomotion that can be explained by quasi-steady modelling, and they broaden the conditions and parameter ranges over which such models are applicable.

Key words: propulsion, flow-structure interactions, swimming/flying

1. Introduction

Flapping locomotion is widespread among flying and swimming animals such as birds, insects, bats and fish, all of which propel through fluids using oscillating wings or fins. Given its ubiquity and the potential for biomimetic propulsion systems, there has been significant interest over recent decades in understanding the relevant fluid dynamical mechanisms. Actively propelled flight as well as unsteady motions of bodies passively falling under gravity have been extensively studied through a confluence of experimental, simulatory, and modelling approaches. Laboratory experiments have involved two-dimensional flow imaging of rigid flapping wings (Birch & Dickinson 2003; Vandenberghe, Zhang & Childress 2004), force sensor measurements of flapping wings (Sane 2001; Sane & Dickinson 2002; Dickson & Dickinson 2004; Wang, Birch & Dickinson 2004), high-speed camera measurements of the trajectories of falling plates (Andersen *et al.* 2005*b*; Huang *et al.* 2013; Li *et al.* 2022), and steady-state measurements of the forces on plates at varying angle of attack (Li *et al.* 2022), among others. Computational fluid dynamics (CFD) simulations have involved direct numerical solves of the Navier–Stokes equations for free-falling plates in two dimensions (Pesavento & Wang 2004; Andersen *et al.* 2005*b*), and for flapping wings in two dimensions (Wang *et al.* 2004) as well as in three dimensions (Sun & Tang 2002; Pohly *et al.* 2018). Mathematical modelling efforts have involved the development of quasi-steady models for insect flight (Sane & Dickinson 2002; Birch & Dickinson 2003; Dickson & Dickinson 2004; Ansari, Żbikowski & Knowles 2006; Wang 2016; Pohly *et al.* 2018) as well as for free-falling plates (Andersen *et al.* 2005*a*,*b*; Pesavento 2006; Hu & Wang 2014; Nakata, Liu & Bomphrey 2015; Li *et al.* 2022; Pomerenk & Ristroph 2025). These experimental, numerical, and modelling studies have together characterised passive and flapping dynamics at an array of intermediate Reynolds numbers.

A major thrust of this line of research aims to use the fluid dynamical effects identified in experiments and simulations to inform mathematical models of the fluid forces. Quasi-steady models (QSMs) in particular express the instantaneous force in terms of the dynamical state of the wing, i.e. its speed and angle of attack, much in the style of conventional lift–drag aerodynamics. Their advantage is the ease and speed in providing predictions in comparison with experiments and CFD simulations, for which it remains challenging to accurately and efficiently assess a wide range of conditions and parameters (Sane & Dickinson 2002; Wang 2016; Pohly *et al.* 2018). The disadvantage of QSMs is the loss of accuracy associated with neglecting inherently unsteady effects, which refer to fundamentally time-dependent phenomena associated with the development of the flow field, including vortex generation and shedding and interactions of the wing with its wake flows. These effects are prevalent at the intermediate Reynolds numbers relevant to animal locomotion and for which the combined actions of viscous and inertial flow effects present challenges to modelling (Wang 2005; Vogel 2008; Klotsa 2019).

Despite their significant approximations and simplifications, QSMs have demonstrated surprising successes for some problems involving locomotion and motion through fluids. Insect flight is a notable example that defied early attempts to account for the forces during hovering using conventional lift–drag estimates but which was later shown to be well described by more elaborate QSMs that included effects such as delayed stall and rotational lift (Sane & Dickinson 2002; Sane 2003; Liu 2005; Ansari *et al.* 2006; Bergou *et al.* 2010; Ristroph *et al.* 2010, 2011, 2013; Shyy *et al.* 2010). Similarly, the dynamics of the 'falling paper problem' involving the passive motions of a falling card, including unsteady motions such as fluttering and tumbling as well as steady gliding, have been reproduced by QSMs that include added mass and dynamic centre of pressure (Andersen *et al.* 2005*a*,*b*; Pesavento 2006; Wang *et al.* 2012; Huang *et al.* 2013; Hu & Wang 2014; Nakata *et al.* 2015; Li *et al.* 2022; Pomerenk & Ristroph 2025). These successes motivate questions about which other flow–structure interaction phenomena might be brought under the purview of QSMs, and in particular whether flapping-based propulsion is amenable to such a treatment.

Archetypal systems for flapping locomotion involve simple wing shapes actuated with simple kinematics. The up-and-down heaving and plunging motions of a thin, flat, rigid plate have been viewed as emblematic of horizontal propulsion in bird-like flight. For a plate of chord length ℓ heaving sinusoidally with frequency f and amplitude a in fluid with density ρ and viscosity μ, the relative strength of inertial to viscous effects can be characterised by the flapping Reynolds number $Re_f = \rho a f \ell/\mu$ (Vandenberghe *et al.* 2004; Alben & Shelley 2005; Lu & Liao 2006). For sufficiently low values of Re_f, experiments and simulations show that the wing flaps in place and does not progress (Vandenberghe *et al.* 2004; Alben & Shelley 2005; Lu & Liao 2006). This stationary state gives way to forward locomotion at higher Re_f via a symmetry-breaking bifurcation in which the wing accelerates and eventually reaches a nearly steady flight speed. Experiments indicate that the transition occurs at a critical $Re_f^* = 20$ to 55 and is accompanied by hysteresis as well as a region of bistability in which both states can be achieved depending on initial conditions (Vandenberghe *et al.* 2004, 2006). Simulations have reported values of Re_f^* in the range of 5 to 50 and with dependencies on the dimensionless amplitude a/ℓ and the solid–fluid density ratio ρ_s/ρ (Alben & Shelley 2005; Lu & Liao 2006). These works interpret the onset of motion as related to interactions of the wing with the vortex flows generated at its edges during each stroke.

For sufficiently high Re_f, the terminal flight speed is observed to scale linearly with the flapping kinematic parameters f and a (Walker 2002; Vandenberghe *et al.* 2004, 2006; Alben & Shelley 2005; Lu & Liao 2006). This outcome is best quantified by the Strouhal number $St = 2af/U$, which represents the ratio of a characteristic speed of flapping to the mean flight speed U. (The numerator is chosen differently in various works, and here we adopt the peak-to-peak amplitude $2a$ as in Alben & Shelley 2005 and elsewhere.) For high Re_f, the Strouhal number undergoes asymptotic convergence to a constant that has been variously reported as $St = 0.1$ to 0.4 (Wang 2000; Nudds, Taylor & Thomas 2004; Alben & Shelley 2005; Lu & Liao 2006; Ramananarivo *et al.* 2016). This range is characteristic of swimming and flying organisms, heaving and pitching plates, and flapping foils, and has been shown by experimental and numerical studies to be associated with optimal thrust production during flapping flight (Taylor, Nudds & Thomas 2003; Nudds *et al.* 2004). Extensive studies of the accompanying flow fields indicate that the selected value of St is closely associated with the inverted von Kármán wake, which consists of vortices of alternating sign that are deposited in an array due to shedding with each stroke (Vandenberghe *et al.* 2004; Alben & Shelley 2005; Lu & Liao 2006; Godoy-Diana, Aider & Wesfreid 2008).

There seems to have been no previous attempt to address the dynamical aspects of flapping propulsion with a QSM. We pursue such here by asking if, despite the clearly documented importance of unsteady effects, the salient phenomena can be reproduced by such a model. If so, what form must it take, and how does this form relate to the previously identified unsteady mechanisms? We focus our investigations on three aspects of the forward dynamics: the state transition from stationary to translating, the time scale defining changes in flight speed from some initial condition, and the speed and Strouhal number characterising the translating state. We embed our efforts within the same class of models that have been developed for and successfully applied to the falling paper problem. Doing so presents the opportunity to unify these different problems under one framework and to potentially extend the sets of conditions over which they are applicable. Wang and coworkers developed models for the two-dimensional (2-D) problem of passive flight of a thin, symmetric plate by accounting for added mass, lift, drag, and their associated torques (Andersen *et al.* 2005*a*,*b*; Pesavento 2006; Wang *et al.* 2012; Huang *et al.* 2013;

Hu & Wang 2014; Nakata *et al.* 2015). Successive iterations have considered wider sets of conditions to drive refinements, including aspects of the centre of pressure, the torque model, rotational lift, and the dependencies of the force coefficients on attack angle (Hover, Haugsdal & Triantafyllou 2004; Huang *et al.* 2013; Li *et al.* 2022; Pomerenk & Ristroph 2025). These developments have generally been done in close connection with CFD simulations and/or experiments and typically in specific contexts that validate the model over limited ranges of Reynolds numbers Re. A key challenge presented by the flapping propulsion problem is the widely ranging $Re = 10$ to 10^5, where lower values mark the onset of vorticity effects and yet higher values are associated with turbulent boundary layer flows (Anderson & Bowden 2005; Schlichting & Gersten 2016).

In the sections that follow, we first introduce a mathematical model whose main innovations pertain to the aerodynamic coefficients and their dependencies on attack angle and Reynolds number. We then survey the key dynamical outputs for representative conditions and show that the model successfully reproduces the known phenomena. Taking advantage of the computational efficiency of the model and its dimensionless representation, we characterise the dynamical outputs with exhaustive sweeps across all conditions of interest. The results identify a critical criterion for take-off, a Strouhal number for steady forward flight and a time scale dictating changes in flight speed, all of which are conserved across wide ranges of conditions. A sensitivity analysis then assesses how the model outputs depend on the values of the constant parameters. Finally, we exploit the mathematical tractability of model to analyse the transition via a linear stability analysis and aspects of the emergent forward flight state via an equilibrium analysis. We conclude by interpreting these findings, suggesting further work along this direction, and speculating about applications of the model to related problems.

2. A quasi-steady model for flapping flight dynamics

2.1. *Model of forward flight dynamics*

We introduce a quasi-steady dynamical model for the driven heaving of a rigid thin plate which is free to move in the direction perpendicular to heaving. To derive such a model, we adopt the form of the QSM that was developed for the passive free flight of a thin wing (Li *et al.* 2022; Pomerenk & Ristroph 2025) and which takes the form of the Newton–Euler equations with forces and torques due to gravity, buoyancy and fluid dynamical effects such as lift, drag, and added mass. The particular case of horizontal motion in a plane and in response to vertical heaving greatly simplifies the aerodynamic considerations by eliminating several degrees of freedom and many of the participating effects. The rotational dynamics need not be evolved because the plate is fixed to lie horizontally in the laboratory frame as in figure 1(*a*): $\theta = \omega = 0$, where θ is the plate orientation angle relative to the horizontal and $\omega = \dot{\theta}$ is the angular velocity. This condition simplifies the translational dynamics by eliminating ω-dependent reference frame terms. The vertical motion is also imposed, rather than evolved, and the position is $y(t) = a\sin(2\pi f t)$ and velocity $v_y(t) = \dot{y} = 2\pi a f \cos(2\pi f t)$ for flapping frequency f and amplitude a. The horizontal flight motion is therefore the only output, leading to a two-variable dynamical system for (x, v_x) that is non-autonomous due to the time-dependent input $v_y(t)$:

$$
\begin{aligned}
\dot{x} &= v_x, \\
\dot{v}_x &= \frac{\rho \ell}{2(m + m_{11})}\sqrt{v_x^2 + v_y^2}\,\big[C_L(\alpha, Re)v_y - C_D(\alpha, Re)v_x\big].
\end{aligned}
\tag{2.1}
$$

https://doi.org/10.1017/jfm.2026.11361 Published online by Cambridge University Press

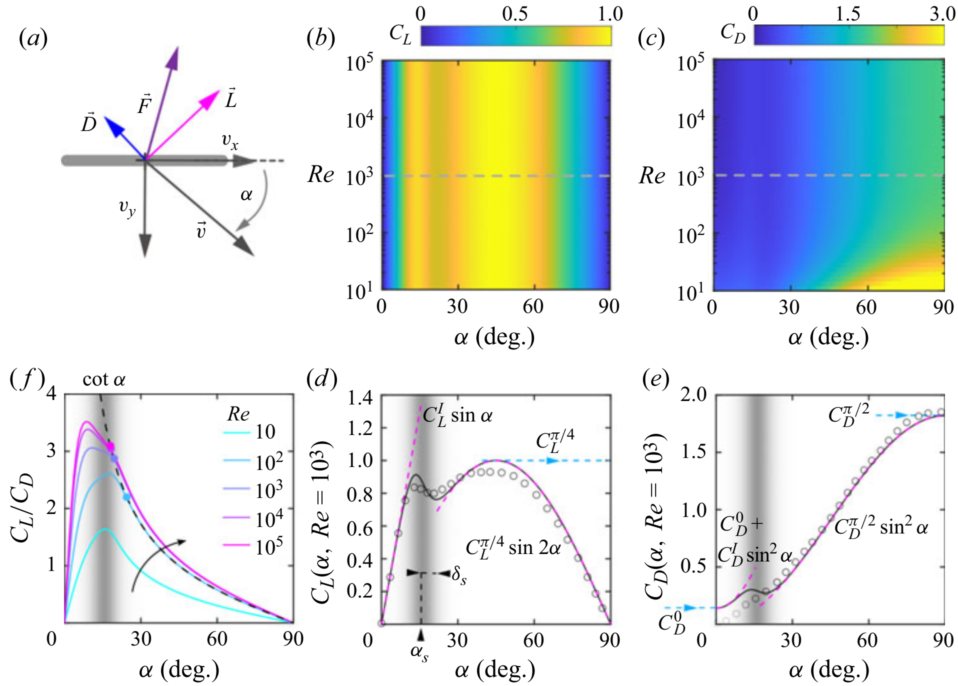

Figure 1. Aerodynamic force coefficients. (*a*) Definitions of dynamical quantities. Shown here during the downstroke, the plate has horizontal and vertical velocity components v_x and v_y that determine the instantaneous attack angle α and Reynolds number *Re*. The total aerodynamic force is resolved into lift and drag. Panels (*b*) and (*c*) show colour maps of lift and drag coefficients $C_L(\alpha, Re)$ and $C_D(\alpha, Re)$. Panels (*d*) and (*e*) show transects of lift and drag coefficients at fixed $Re = 10^3$. Dashed magenta curves and the accompanying equations represent the mathematical forms applicable to the attached flow regime at small α and the separated flow regime at high α. The grey band shows the transitional region where stall occurs. Dashed blue lines and accompanying labels highlight some parameter values. Open black circles indicate experimental measurements from Li *et al.* (2022). (*f*) The lift-to-drag ratio C_L/C_D with respect to α at logarithmically spaced *Re*. The graph of $\cot\alpha$ (black dashed curve) and the marked intersections relate to an equilibrium analysis.

Here, x and y are laboratory frame coordinates of the plate centre or any other arbitrary reference point on the body. The plate has chord length ℓ and mass m per unit length along the span. The fluid has density ρ, and the added mass coefficient m_{11} (also per unit span) is associated with edgewise motions of the plate (Andersen *et al.* 2005*b*).

Notably, the dominant aerodynamic effect that remains is the force associated with translation, which is decomposed into lift and drag components and expressed in the usual high-*Re* form with force coefficients C_L and C_D. Figure 1(*a*) shows a force diagram at an arbitrary instant. The force coefficients are in general expected to vary with both the attack angle $\alpha = \arctan(v_y/v_x)$ and Reynolds number $Re = \rho\ell\sqrt{v_x^2 + v_y^2}/\mu$, where μ is the fluid viscosity coefficient. These quantities vary in time and, due to the involvement of v_x, are outcomes of the solution. The mathematical forms for the coefficients $C_L(\alpha, Re)$ and $C_D(\alpha, Re)$ dictate the behaviour of the system and thus whether such a model reproduces the key dynamical features of flapping locomotion. If at all successful, one expects such a model to reproduce forces averaged over times longer than a wing stroke period $1/f$ and hence aspects of the flight dynamics over similarly long time scales. As a quasi-steady treatment, many effects are treated only approximately through the specified force coefficients, and many are neglected altogether. The key assumption that the instantaneous force during unsteady motions is taken as the time-averaged force for the corresponding steady condition (i.e. same speed and attack angle) is not rigorously justified *a priori* and hence must be assessed by comparing model outputs with known results. Intrinsically unsteady phenomena such as fluctuating forces from vortex shedding are not included (Wang 2000).

2.2. *Dimensionless form of the model and its outputs*

Comparison across different parameter values is facilitated by non-dimensionalisation of (2.1). Following earlier works, we choose characteristic scales for length ℓ, time $1/f$, and thus speed ℓf (Alben & Shelley 2005; Spagnolie *et al.* 2010). Let $v_x' = v_x/(\ell f)$, $x' = x/\ell$, likewise for v_y' and y', and $t' = tf$. Then the imposed driving takes the form $y' = A\sin(2\pi t')$ and $v_y' = \dot{y}'$ for the dimensionless amplitude $A = a/\ell$. The dynamics transform as

$$\begin{aligned} \dot{x}' &= v_x', \\ \dot{v}_x' &= \frac{1}{2M}\sqrt{(v_x')^2 + (v_y')^2}\left[C_L(\alpha, Re)v_y' - C_D(\alpha, Re)v_x'\right], \end{aligned} \tag{2.2}$$

where $M = (m + m_{11})/\rho\ell^2$ is the dimensionless mass that normalises the combined solid and added masses (per unit span) by a relevant mass of fluid.

The coefficients C_L and C_D are themselves dimensionless and expressed in terms of dimensionless quantities. The angle of attack α assumes the same form whether dimensional or dimensionless. The dynamical or instantaneous Reynolds number transforms as $Re = \rho\ell\sqrt{v_x^2 + v_y^2}/\mu = \rho\ell^2 f\sqrt{v_x'^2 + v_y'^2}/\mu = (Re_f/A)\sqrt{v_x'^2 + v_y'^2}$, where the flapping Reynolds number is $Re_f = \rho\ell a f/\mu$. The system is therefore characterised by three dimensionless input parameters: $M = (m + m_{11})/\rho\ell^2$, $A = a/\ell$, and $Re_f = \rho\ell a f/\mu$. The outputs are the dynamics $(x', v_x') = (x/\ell, v_x/\ell f)$, the results of which will be analysed to extract summary quantities.

2.3. *Specification of aerodynamic force coefficients*

Lift and drag coefficients for thin rectangular plates have been reported for certain ranges of attack angles and isolated Reynolds numbers (Tomotika & Aoi 1953; Sane & Dickinson 2001; Andersen *et al.* 2005*a*; Ehrenstein & Eloy 2013; Bhati *et al.* 2018; Li *et al.* 2022). Based on these partial characterisations, we propose mathematical forms for $C_L(\alpha, Re)$ and $C_D(\alpha, Re)$ that capture the known flow phenomenology and which involve constant parameters whose values can be informed by reported aerodynamic data. These forms are:

$$C_{L,D}(\alpha, Re) = f(\alpha, Re)C^A_{L,D}(\alpha, Re) + \left[1 - f(\alpha, Re)\right]C^S_{L,D}(\alpha, Re)$$

$$\text{where} \quad f(\alpha, Re) = \frac{1}{2}\left[1 - \tanh\frac{\alpha - \alpha_S(Re)}{\delta_S(Re)}\right] \quad \text{with} \quad \alpha_S = 15^\circ, \quad \delta_S = 5^\circ.$$

Attached flow coefficients:

$$C^A_L(\alpha, Re) = C^I_L(Re)\sin\alpha \quad \text{with} \quad C^I_L = 5$$

$$C^A_D(\alpha, Re) = C^0_D(Re) + C^I_D(Re)\sin^2\alpha \quad \text{with} \quad C^I_D = 5$$

$$\text{where} \quad C^0_D(Re) = C^{0,FT}_D + \frac{C^{0,SF}_D}{\sqrt{Re}} \quad \text{with} \quad C^{0,FT}_D = 0.1, \quad C^{0,SF}_D = 1.3.$$

Separated flow coefficients:

$$
\begin{aligned}
&C_L^S(Re) = C_L^{\pi/4}(Re)\sin 2\alpha \quad \text{with} \quad C_L^{\pi/4} = 1\\
&C_D^S(Re) = C_D^{\pi/2}(Re)\sin^2\alpha\\
&\quad\text{where} \quad C_D^{\pi/2}(Re) = C_D^{\pi/2,HR} + \frac{C_D^{\pi/2,LR}}{Re} \quad \text{with} \quad C_D^{\pi/2,HR} = 1.8, \quad C_D^{\pi/2,LR} = 20.
\end{aligned}
\tag{2.3}
$$

These equations represent surfaces $C_L(\alpha, Re)$ and $C_D(\alpha, Re)$ that are plotted in figures 1(*b*) and 1(*c*). The attack angle $\alpha \in [0, \pi/2] = [0, 90°]$ is shown over the conventional aerodynamic range, and the coefficients are readily extended over all possible orientations $\alpha \in [0, 2\pi)$ by consideration of the dual symmetries of the plate (Li *et al.* 2022). The displayed range of the Reynolds number $Re \in [10, 10^5]$ reflects the intermediate regime over which the model can be expected to apply. The lift map is strictly uniform with respect to Re, and the drag map is largely so except for notable variations at lower values. The forces vary with α in ways that are more clearly seen in the transects of figures 1(*d*) and 1(*e*) at a representative $Re = 10^3$, and these panels graphically interpret the terms and parameters in the model equations. Comparison with the experimental measurements (open circles) of Li *et al.* (2022) shows good agreement in the forms of the curves while not faithfully reproducing all features of the data. Note that these experiments reflect only pressure-based or normal forces and hence the measured C_D at low angles $\alpha < \alpha_S$ (faded data points) are underestimates that neglect skin friction as a force tangential to the plate (Li *et al.* 2022). Additional checks against experimental and computational studies at $Re = 10^2$ (Wang *et al.* 2004) and $Re = 10^5$ (Ananda, Sukumar & Selig 2015) indicate good agreement for low angles and generally at the level of trends in the curves and rough magnitudes.

The equations (2.3) above are structured to reflect the program we have used for specifying the coefficient formulas. First, we assume two distinct aerodynamic regimes which are respectively associated with attached flow for low α and fully separated flow at high α. The function $f(\alpha, Re)$ serves the role of selecting the regime. It is the sigmoid-shaped logistic curve that takes on values near 1 for low α, drops near α_S, and approaches 0 for high α. The critical angle α_S marks the stall transition, and the factor δ_S specifies the angular width or range over which the transition occurs. Both may in principle depend on Re, but available data at $Re = 10^3$ and 10^5 show stall to occur over the range $\alpha = 10°$ to $20°$, hence our choices for the constant values $\alpha_S = 15°$ and $\delta_S = 5°$ (Ananda *et al.* 2015; Li *et al.* 2022). The transitional region is marked by grey stripes in figures 1(*d*) and 1(*e*).

Next, we set about specifying the coefficients $C_{L,D}^A(\alpha, Re)$ for the attached flow regime, focusing first on the dependence on α then Re. The lift coefficient $C_L^A \propto \sin\alpha$ follows the form of Kutta–Joukowski theory for thin wings (Anderson 2011) and is consistent with measurements at various Re showing approximately linear increase in lift with attack angle for low α (Ananda *et al.* 2015; Li *et al.* 2022). The prefactor $C_L^I(Re)$ is the slope or inclination of the lift curve at small α, and it may in principle depend on Re. Its value is 2π in potential flow theory (Anderson 2011; Gutierrez-Castillo *et al.* 2021), and experimental studies across widely ranging $Re = 10^2$ to 10^5 report somewhat lower values between 4 and 6 with no systematic dependence on Re (Ananda *et al.* 2015; Gutierrez-Castillo *et al.* 2021; Li *et al.* 2022). Hence we choose the constant $C_L^I(Re) = 5$ as a representative value across all Re. The drag model $C_D^A(\alpha, Re)$ has two terms, the first of which represents the fluid resistance present for edgewise motions at $\alpha = 0$. It involves the constant term that represents the (small) pressure drag associated with the finite thickness of the plate (Anderson & Bowden 2005; Andersen *et al.* 2005*b*). It is expected to be of the same order as the thickness-to-chord ratio, and the value $C_D^{0,FT}=0.1$ is chosen as typical of wing plates considered in previous studies (Taylor *et al.* 2003; Vandenberghe *et al.* 2004; Andersen *et al.* 2005*a*; Alben & Shelley 2005; Li *et al.* 2022). The second term captures the effect of skin friction, and the prefactor value $C_D^{0,SF}=1.3$ and scaling as $1/\sqrt{Re}$ are the classical results of the Blasius boundary-layer theory calculation (Tomotika & Aoi 1953; Bhati *et al.* 2018). The second term in $C_D^A(\alpha, Re)$ represents lift-induced drag, which arises due to the change in effective attack angle due to lift generation (Anderson & Bowden 2005; Anderson 2011). Its form as $\sin^2\alpha$ reflects the quadratic dependence on the lift coefficient according to Prandtl's lifting-line theory (Anderson & Bowden 2005; Gutierrez-Castillo *et al.* 2021), which also predicts the constant prefactor to depend on the span-to-chord aspect ratio. The chosen value $C_D^I=5$ was determined empirically in Li *et al.* (2022) for plates with aspect ratios of 5 to 10.

We carry out similar procedures for the coefficients $C_{L,D}^S(\alpha, Re)$ in the separated flow regime applicable to high angles beyond the stall transition. Considering lift, the dependence on α of $C_L^S\propto\sin 2\alpha$ has been adopted in previous modelling work and reflects the observation that lift tends to be maximal near $\alpha=\pi/4=45^\circ$ and fall off toward lower and higher values, as expected by symmetry (Andersen *et al.* 2005*b*; Li *et al.* 2022). The maximal value of the lift coefficient has been reported to be 0.7 to 1.3 in studies across widely ranging Re, motivating our choice of the constant $C_L^{\pi/4}=1$ (Andersen *et al.* 2005*b*; Ananda *et al.* 2015; Li *et al.* 2022). Considering drag, the dependence $C_D^S\propto\sin^2\alpha$ has similarly been used previously (Andersen *et al.* 2005*b*; Li *et al.* 2022) and models the observed monotonic increase up to $\alpha=\pi/2=90^\circ$. The maximal value of $C_D^{\pi/2}(Re)$ is the drag coefficient for a plate in normal flow, which for bluff bodies is constant at higher Re and scales as $1/Re$ at low Re (Jones & Knudsen 1961; Bhati *et al.* 2018). The associated values $C^{\pi/2,HR}=1.8$ and $C^{\pi/2,LR}=20$ are chosen as fits to measurements across $Re\in(10, 10^8)$ (Bhati *et al.* 2018).

In summary, the lift and drag coefficients $C_{L,D}(\alpha, Re)$ have functional dependencies on attack angle and Reynolds number that are informed by aerodynamic theory. They involve 9 constants whose values are informed by previous measurements: $\alpha_S=15^\circ$, $\delta_S=5^\circ$, $C_L^I=5$, $C_D^{0,FT}=0.1$, $C_D^{0,SF}=1.3$, $C_D^I=5$, $C_L^{\pi/4}=1$, $C_D^{\pi/2,HR}=1.8$, $C_D^{\pi/2,LR}=20$. The first two define the stall transition, the following four define the attached flow regime for small α, and the last three define the separated flow regime for large α.

3. Characterisation of flight dynamical behaviours

Here, we characterise the dynamical behaviours resulting from numerical solutions of the proposed QSM and thereby demonstrate that it closely reproduces the key characteristics of flapping-based propulsion. To this end, equations (2.2) are integrated numerically in time via MATLAB's built-in solver *ode15s* that is optimised for systems of stiff ordinary differential equations. Its algorithm is based on numerical differentiation formulas up to fifth order, and variable time stepping ensures a specified degree of accuracy. Convergence tests determine the values of the relative $\mathrm{RelTol}=10^{-10}$ and absolute $\mathrm{AbsTol}=10^{-9}$ tolerances used for all results presented here. The initial condition for the translational speed is $v_x'(0)=0.01$, which represents a small perturbation whose purpose is to break the left–right symmetry. We choose $M=A=1$ for simplicity here, and the effects of varying these parameters will be systematically assessed in the next section.

Figure 2(*a*) displays curves of the dimensionless displacement $x'=x/\ell$ over time for logarithmically increasing $Re_f=10, 10^2, \ldots, 10^5$, where each curve is associated with a different fixed Re_f that increases from left to right. The initial positions are spaced

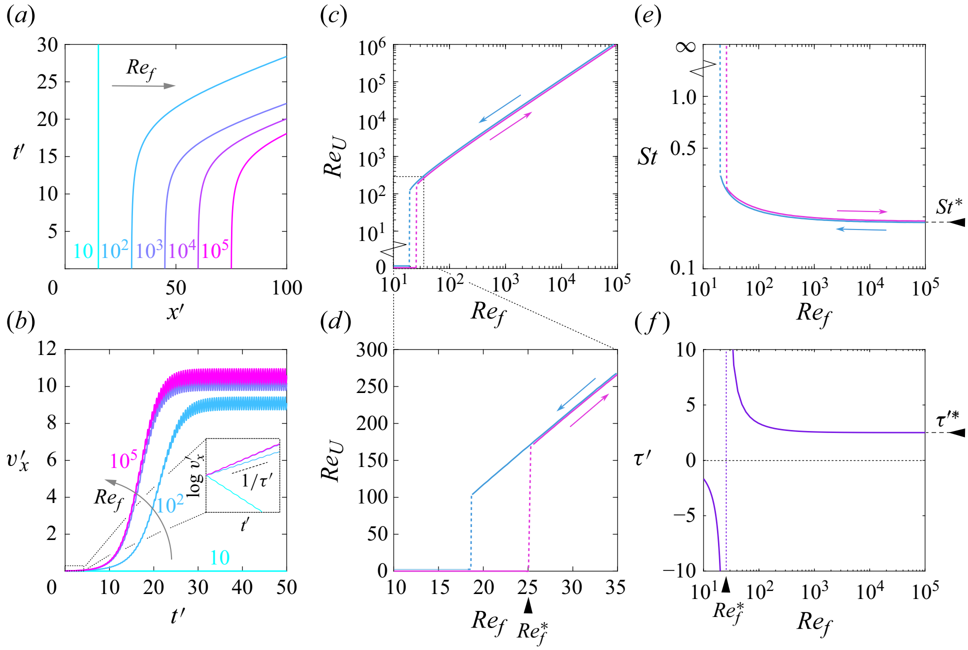

Figure 2. Model dynamics reproduce characteristic flapping flight behaviours. (*a*) Dimensionless position x' versus t' for the indicated values of Re_f. (*b*) Dimensionless horizontal speed against time. Inset: log–linear plot for early times. (*c*) Terminal flight speed versus flapping frequency, shown in dimensionless forms as the horizontal Reynolds number Re_U against Re_f. Low Re_f leads to a stationary state, while higher Re_f yields forward flight following a linear relation $Re_U \propto Re_f$. (*d*) Magnified view for low Re_f showing hysteresis and bistability at the transition to forward flight. Stability of the stationary state is lost at the critical value $Re_f^* = 25$. (*e*) Strouhal number St plotted against Re_f, with the value $St^* = 0.2$ characterising $Re_f \gg Re_f^*$. (*f*) Dimensionless exponential time scale τ' plotted against Re_f, where the sign of τ' indicates decay (−) or growth (+) of speed and hence stability or instability of the stationary state. The change of sign indicates the state transition at $Re_f^* = 25$, and the limiting value $\tau'^* = 2.5$ characterises $Re_f \gg Re_f^*$.

apart for ease of visibility. For small $Re_f = 10$ (left vertical line, cyan), the plate remains stationary for all time. In contrast, higher $Re_f \geqslant 100$ (right curves, darker cyan and magenta) induces the plate to take off into forward flight. Figure 2(*b*) presents these same simulation results in terms of dimensionless speeds v'_x over time for the same choices of Re_f. Evidently, flapping of a plate induces one of two possible terminal or long-time behaviours determined by the value of the flapping Reynolds number. For low Re_f, the plate assumes a stationary state in which it flaps in place with no forward progression. For moderate to high Re_f, it reaches a forward flight state characterised by constant stroke-averaged translational speed with relatively small fluctuations within each stroke. The inset of figure 2(*b*) is a rescaled log–linear plot of the early-time data, from which it is evident that the speed either decays (negatively sloped cyan curve, $Re_f = 10$) or grows (positively sloped curves, $Re_f = 10^2$ to 10^5) exponentially from its initial value.

Further details regarding the terminal states and the transition are provided in figure 2(*c*) and the magnified view of panel (*d*). Here the mean speed $U = \overline{v}_x = \overline{v}'_x \ell f$ during the terminal state is used to compute the forward flight Reynolds number $Re_U = \rho U \ell / \mu$ based on the horizontal motion. Panel (*c*) reports the output motion Re_U versus the input flapping Reynolds number Re_f, revealing a linear relationship for sufficiently large Re_f. The more complex behaviour at low Re_f is clarified by the zoomed-in view in (*d*), which reveals a

Quantity	Current study	Previous study	Reference
Re_f^*	25	20 to 55	Vandenberghe *et al.* (2004)
		15 to 50	Alben & Shelley (2005)
St^*	0.2	0.2 to 0.4	Taylor *et al.* (2003)
		0.21 to 0.25	Nudds *et al.* (2004)
		0.15 to 0.2	Alben & Shelley (2005)

Table 1. Comparison of predictions from the current study for the quantities Re_f^* and St^* against previously reported values from experiments and direct numerical simulations.

hysteresis loop that brackets a range of bistability in which the stationary and forward flight states coexist. This structure is revealed by a procedure in which we incrementally increase Re_f in a stepwise fashion, where each step is initialised with the previous step's flight speed and Re_f is held constant for sufficiently long that the forward dynamics equilibrate and Re_U can be extracted. The results of this upward sweep are shown as the magenta curve, and it is followed by a downward sweep shown in cyan. These data identify a lower value $Re_f = 18$ below which only the stationary state is observed and a higher value of 25 above which only the forward flight state is seen. As summarised in table 1, these results can be compared with the hysteretic dynamics reported in previous experiments to occur around $Re_f = 20$ to 55 (Vandenberghe *et al.* 2004), as well as the more complex transition to locomotion seen in numerical simulations around $Re_f = 15$ to 50 (Alben & Shelley 2005).

These same data are recast in figure 2(*e*) in terms of the Strouhal number $St = 2af/U = 2Re_f/Re_U$ attained across varying Re_f. Beyond the onset to locomotion, St rapidly drops to approximately 0.3 and thereafter changes little as it asymptotically approaches a constant value near $St^* = 0.2$ for large Re_f, where $St^* = St(Re_f \gg Re_f^*)$. As summarised in table 1, these results can be compared with the range $St = 0.15$ to 0.4 that has been reported to apply to the cruising flight and steady swimming of many diverse animals and which has been associated with efficient flapping locomotion (Taylor *et al.* 2003; Nudds *et al.* 2004; Alben & Shelley 2005).

Lastly, we characterise the time scale associated with the observed exponential decay or growth of the flight speed at early times. Building on the analysis shown in the inset of figure 2(*b*), we fit lines to the log–linear data of $v_x'(t')$ across values of Re_f and associate the inverse of the slope with the decay/growth time scale τ'. Negative values $\tau' < 0$ are associated with decay and hence stability of the stationary state, and positive $\tau' > 0$ with growth and thus instability that drives the body into forward flight. The extracted data $\tau'(Re_f)$ are shown as the curve in figure 2(*f*). These results identify the critical value $Re_f^* = 25$ (vertical dotted line) below which $\tau' < 0$ and above which $\tau' > 0$. This value matches to the upper bound for the hysteretic region as detailed in figure 2(*d*), and this correspondence is understood by noting that both results pertain to the loss of stability of the stationary state. These findings indicate that the sign change of τ' can be used generally to identify the transitional value Re_f^* that is shown here to be 25 for $M = A = 1$ and whose characterisation across the parameter space is taken up in the next section. Further, for large $Re_f \gg Re_f^*$ the time scale asymptotically approaches a constant value $\tau'^* = \tau'(Re_f \gg Re_f^*)$, and its parametric dependence will be assessed in what follows. We are not aware of previous studies characterising this time scale, and hence the results presented here are predictions that may be compared with the results of future experiments and simulations.

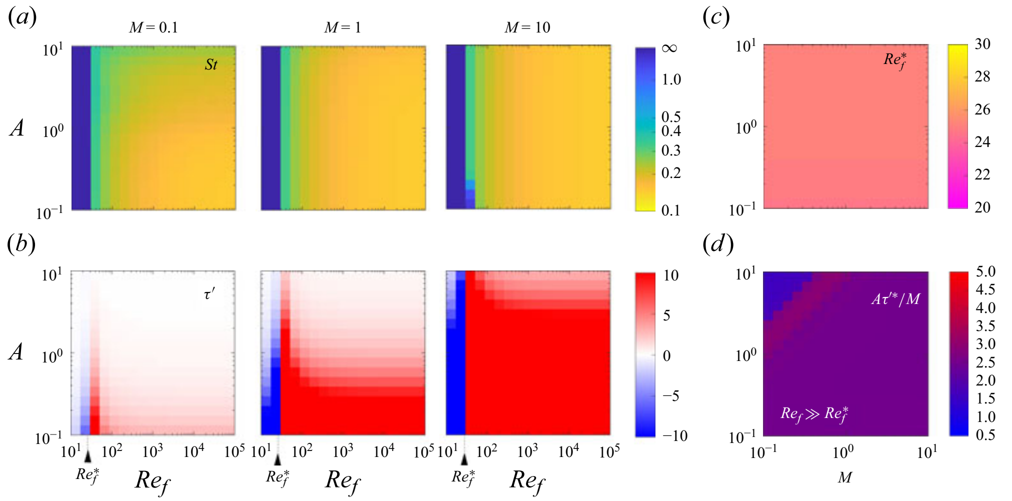

Figure 3. Tableau characterising the dependencies of the key output quantities on the input parameters M, A, and Re_f. Each pixel in a given map corresponds to a run of the simulation at the indicated parameter values. Panels (*a*) and (*b*) show the Strouhal number St and characteristic growth/decay time τ'. The former is nearly constant with value $St^* = 0.2$ for large Re_f and across all M and A. (*c*) The critical value Re_f^*, defined as the point at which τ' changes sign. This is a nearly constant field in M and A with $Re_f^* = 25$. (*d*) The rescaled growth/decay time scale $A\tau'^*/M$ for fixed $Re_f = 10^5 \gg Re_f^*$ displays a nearly uniform map, implying that $\tau'^* \approx 2.5M/A$.

4. Characterisations across physical and kinematic parameters

Having confirmed the model's ability to reproduce the key phenomena for the intermediate values $M = A = 1$, we next conduct a sweep throughout the full space of the physical and kinematic input parameters M, A and Re_f. The output quantities of interest include: the terminal Strouhal number St attained, the characteristic growth or decay time scale τ', and the critical bifurcation parameter Re_f^* that marks the transition from the stationary state to forward flight. It will also be of interest to consider the high-Re_f asymptotic values of the former two parameters: $St^* = St(Re_f \gg Re_f^*)$ and $\tau'^* = \tau'(Re_f \gg Re_f^*)$. The results are compiled in figure 3. The explored values $M \in \{0.1, 1, 10\}$, $A \in [0.1, 10]$ and $Re_f \in [10, 10^5]$ are chosen to span the wide-ranging parameters applicable to flapping-based swimming and flight of animals (Pennycuick 1996; Taylor *et al.* 2003; Vandenberghe *et al.* 2004; Fish *et al.* 2016; Kang *et al.* 2018).

Displayed in the panels of figure 3(*a*) are terminal values of St, where each panel scans the space of (Re_f, A) and the three panels correspond to $M = 0.1$, 1 and 10. For lower values of Re_f below the transition, the stationary state prevails and $St \to \infty$ (dark blue) across all values of M and A. For higher values of Re_f beyond the transition, the Strouhal number abruptly reaches finite values and saturates to the selected value of approximately $St^* = 0.2$ (yellow-orange). In this regime, St shows only minor variations with M and A. These results seem to corroborate the view that forward flapping flight dynamics are universal in the sense that this key metric is conserved across the vast majority of the parameter space (Taylor *et al.* 2003; Nudds *et al.* 2004; Alben & Shelley 2005; Ramananarivo *et al.* 2016).

Displayed in the panels of figure 3(*b*) are the dimensionless growth/decay times τ'. Across all M and A, it is seen that $\tau' < 0$ (blue tones) for sufficiently low $Re_f < Re_f^*$ and

$\tau' > 0$ (red tones) for higher $Re_f > Re_f^*$. Thus, the existence of the transition from the stationary state to locomotion is maintained for all conditions, and the transitional value Re_f^* itself appears similarly preserved. To assess this quantitatively and systematically across the space, we extract $Re_f^*(M, A)$ via the change of sign in τ' and compile the results in the map of figure 3(*c*). The panel is notably uniform in colour, indicating that the value of the critical flapping Reynolds number is highly conserved near $Re_f^* = 25$. Additional investigations indicate that the value $Re_f = 18$ marking the lower boundary of the hysteresis window is also conserved across M and A.

Further, comparisons within each panel of figure 3(*b*) show that $|\tau'|$ generally decreases (lighter tones) with A, and comparisons across the panels show that $|\tau'|$ increases (darker tones) with M. This suggests a relationship of the form $\tau'(M, A) \sim M/A$, and indeed rescaling as $A\tau'/M$ proves to largely remove the variations, as shown by the map of figure 3(*d*). Here, we fix $Re_f = 10^5$ as representative of $Re_f \gg Re_f^*$, and it is seen that $A\tau'^*/M$ falls within a narrow range of 1 to 3 as M and A are each varied over two orders of magnitude.

In summary, these parametric sweeps reveal three quantities that are highly conserved: (i) the selected Strouhal number $St^* = 0.2$ holds for sufficiently high $Re_f > Re_f^*$ and across all M and A; (ii) the rescaled dynamical time scale $A\tau'^*/M = 2 \pm 1$ similarly holds; and (iii) the critical Reynolds number $Re_f^* = 25$ holds for all M and A. The significance of these results is that they support the view that some key dynamical features are common to flapping-based propulsion across wide ranges of physical conditions, parameter values, and scales. Such universality has been recognised previously with respect to the Strouhal number and to some degree the critical Reynolds number, and future studies may now investigate the newly identified time scale.

5. Sensitivity analysis of model parameters

We next conduct a sensitivity analysis of the constant parameters appearing in the aerodynamic model in order to determine their influence on the dynamical outputs. Specifically, the full slate of parameters include the 9 constants C_L^I, $C_D^{0,FT}$, $C_D^{0,SF}$, C_D^I, α_S, δ_S, $C_L^{\pi/4}$, $C_D^{\pi/2,HR}$, and $C_D^{\pi/2,LR}$, the first 4 of which pertain to the attached flow regime, the next 2 to the stall transition and the last 3 to the separated flow regime. The dynamical outputs of interest are Re_f^*, τ'^*, and St^*. For the purpose of this analysis, we consider fixed values $M = A = 1$, which should be viewed as generally representative given that the outputs are highly conserved. Similarly, we consider fixed $Re_f = 10^5$ as representative of conditions $Re_f \gg Re_f^*$ where the asymptotic values St^* and τ'^* are attained. We define a dimensionless sensitivity score to each output quantity Q with respect to each input parameter p

$$S_{Q,p} = \left| \frac{\partial Q}{\partial p} \frac{p_0}{Q_0} \right| \approx \left| \frac{\Delta Q/Q_0}{\Delta p/p_0} \right|. \tag{5.1}$$

Here, p_0 is the nominal parameter value and $Q_0 = Q(p_0)$ is the associated nominal value of the output quantity extracted from the numerical solution. The difference approximation to the derivative allows the score to be estimated by running computations for a perturbed parameter value $p = p_0 + \Delta p$ and extracting the change $\Delta Q = Q - Q_0$ in the output quantity. We implement a two-sided approximation by averaging the results of perturbations of size $\pm 10\,\%$ in each parameter, i.e. $\Delta p = \pm 0.1 p_0$.

https://doi.org/10.1017/jfm.2026.11361 Published online by Cambridge University Press

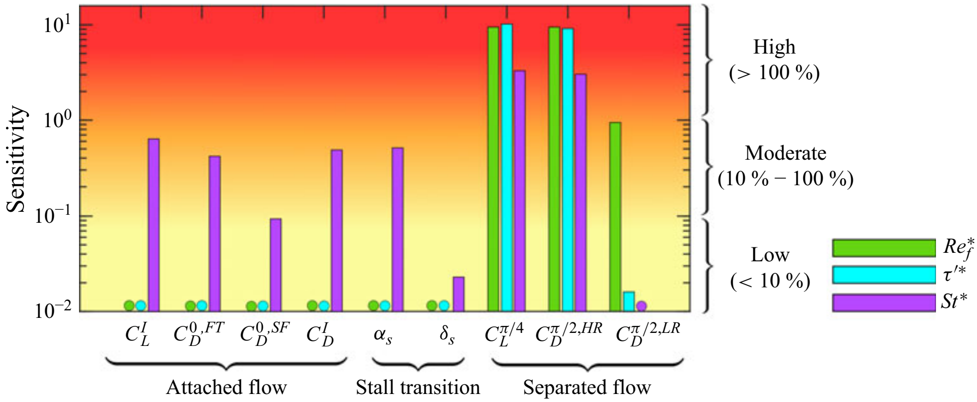

Figure 4. Sensitivity of the dynamical outputs to the constant parameters in the aerodynamic model. The relevant quantities include the critical Re_f^* (green), characteristic growth/decay time scale τ'^* (cyan), and terminal Strouhal number St^* (purple). Here, the dimensionless mass and amplitude are fixed with $M = A = 1$, and $Re_f = 10^5 \gg Re_f^*$ for the results pertaining to St^* and τ'^*. Sensitivity scores less than 1 % are not displayed and instead marked with dots.

The results of this analysis are displayed as the bar chart of figure 4 showing the sensitivities of Re_f^* (green), τ'^* (cyan), and St^* (purple) with respect to the 9 aerodynamic parameters. Here, scores less than $0.1 = 10\,\%$ can be considered low and hence the output is robust to changes in the parameter, and scores above $1 = 100\,\%$ are high and signify a strong dependency. Moderate sensitivity occurs for intermediate values, and very low scores below $0.01 = 1\,\%$ are not displayed and instead marked with dots. Evidently, the quantities Re_f^* and τ'^* display sensitivity only to the coefficients $C_L^{\pi/4}$, $C_D^{\pi/2,HR}$, and $C_D^{\pi/2,LR}$, which are the subset that govern the separated flow regime. This suggests that the aerodynamics associated with attached flow and stall does not play a role in the stationary-to-locomotion transition. In contrast, the Strouhal number St^* is broadly sensitive to nearly all parameters at levels that are at least moderate. Thus, it seems that the mechanisms associated with attached flow, stall and separated flow are all important determinants of St^*. These observations are explained by the equilibrium and stability analyses provided in the next section.

It should be noted that nearly all 9 parameters affect at least one output quantity at a moderate level of 10 % or greater. The exception is δ_S, which defines the angular breadth of the stall transition and displays uniformly low sensitivities. Even this parameter is necessary to include in the model in order to mathematically specify the cross-over between the flow regimes, but apparently the outputs are robust to its numerical value. Taken together, these results indicate that the model is minimal in the sense of containing no unnecessary parameters.

6. Interpretations via equilibrium and stability analyses

The tractability of the quasi-steady formulation allows for analytical insights into key features of the dynamics, and we first seek interpretations for the critical Reynolds number Re_f^* for take-off from rest and the characteristic dimensional time scale τ to reach the terminal locomotion state. Our theory is based on the linear stability of the stationary state, for which the attack angle is high and we may safely assume the separated flow forms of the lift and drag coefficients. It proves adequate to focus on one stroke in the flapping cycle and assume steady vertical motion $v_y \cong \bar{v}_y = 4af$ which here is chosen to be the mean speed. Perturbation of the flight speed introduces the small parameter $\varepsilon = v_x/v_y \ll 1$ whose dynamics we seek through equation (2.1). The terms involve $v = \sqrt{v_x^2 + v_y^2} = v_y\sqrt{\varepsilon^2+1} \cong v_y$ and $Re = \rho \ell v/\mu \cong \rho\ell v_y/\mu \cong 4\rho\ell af/\mu = 4Re_f$, where the symbol '$\cong$' is used wherever the steady motion approximation or linearisation in ε is invoked. Inputting the attack angle $\alpha \cong \pi/2 - \varepsilon$ yields the coefficients of lift $C_L^S(Re,\alpha) = C_L^{\pi/4}\sin 2\alpha \cong C_L^{\pi/4}\sin(\pi - 2\varepsilon) \cong 2C_L^{\pi/4}\varepsilon$ and drag $C_D^S(Re,\alpha) = (C_D^{\pi/2,HR} + C_D^{\pi/2,LR}/Re)\sin^2\alpha \cong (C_D^{\pi/2,HR} + C_D^{\pi/2,LR}/4Re_f)\sin^2(\pi/2-\varepsilon) \cong C_D^{\pi/2,HR} + C_D^{\pi/2,LR}/4Re_f$. Inserting all these forms into equation (2.1) and simplifying yields an expression for the linearised dynamics:

$$\dot{\varepsilon} = \tau^{-1}\varepsilon \Rightarrow \varepsilon(t) = \varepsilon_0 e^{t/\tau}, \tau^{-1} = \frac{1}{2}\frac{\rho\ell v_y}{m+m_{11}}\left[2C_L^{\pi/4} - \left(C_D^{\pi/2,HR} + \frac{C_D^{\pi/2,LR}}{4Re_f}\right)\right]. \tag{6.1}$$

Hence, the perturbation is predicted to decrease or increase according to the sign of τ, which is the associated exponential decay or growth time scale. Notably, $\tau < 0$ for sufficiently small Re_f, indicating that the stationary state is stable, whereas $\tau > 0$ for larger Re_f and the wing takes off into forward flight. The critical value Re_f^* marking the transition is determined by $\tau^{-1}(Re_f^*) = 0$:

$$Re_f^* = \frac{C_D^{\pi/2,LR}}{4(2C_L^{\pi/4} - C_D^{\pi/2,HR})} = 25, \tag{6.2}$$

where the computed result reflects the nominal set of model parameters. This matches the critical value identified in the numerical results presented in §§ 3 and 4.

These results interpret the take-off condition for forward flight as requiring sufficiently high Reynolds number such that the horizontal component of lift exceeds drag at high attack angles, thereby generating a forward directed force vector that destabilises the stationary state. The expression (6.2) also explains why the critical Reynolds number is almost entirely independent of M and A per the results of figure 3(*c*), and why it is sensitive to the three aerodynamic coefficients $C_L^{\pi/4}$, $C_D^{\pi/2,HR}$, and $C_D^{\pi/2,LR}$ of the separated flow regime and insensitive to the other model parameters per the results of figure 4. Similarly, this analysis interprets the time scale τ via equation (6.1) as arising from the inertial resistance to motion in response to the aerodynamic forces. The dimensionless form and its limit for $Re_f \gg Re_f^*$ are

$$(\tau')^{-1} = 2\frac{A}{M}\left[2C_L^{\pi/4} - \left(C_D^{\pi/2,HR} + \frac{C_D^{\pi/2,LR}}{4Re_f}\right)\right] \to 2\frac{A}{M}\left(2C_L^{\pi/4} - C_D^{\pi/2,HR}\right) = \frac{A}{2.5M}. \tag{6.3}$$

This explains why the rescaled quantity $A\tau'^*/M$ is nearly conserved as shown in figure 3(*d*), and the predicted value of 2.5 corresponds well with the range of 1 to 3 seen in the numerical results. The above expression also explains the sensitivity of τ'^* to the separated flow parameters and insensitivity to all others per figure 4.

A similar attempt to account for the selected Strouhal number views the forward flight state as arising from a balance of horizontal forces in which the forward-inclined lift vector balances the rearward-pointing drag. We again assume constant $v_y \cong 4af$, but v_x cannot be assumed to be small. Equilibrium requires that $C_L(\alpha, Re)\sin\alpha = C_D(\alpha, Re)\cos\alpha$ and hence $C_L(\alpha, Re)/C_D(\alpha, Re) = \cot\alpha$. This condition represents an implicit relation for the unknown v_x, which appears in the attack angle $\tan\alpha = v_y/v_x \cong 4af/v_x = 2St$ and Reynolds number $Re = \rho\ell\sqrt{v_x^2 + v_y^2}/\mu$. The equilibrium solutions are those α marking the intersections shown in figure 1(f). Further analytical progress is hindered because the dynamically selected values $\alpha = 18°$ to $27°$ fall in or near the stall range, necessitating consideration of the full forms of C_L and C_D including the stall parameters and those of the attached and separated flow regimes. Nonetheless, the relatively narrow range of α across all $Re > Re_f^*$ implies a similarly conserved Strouhal number $St^* \cong (\tan\alpha)/2 = 0.16$ to 0.21, which aligns with the findings of figures 2(e) and 3(a). Further, that the associated attack angles span the flow regimes explains why St^* is sensitive to the full array of model parameters per figure 4. We also note that these complexities similarly hinder any analytical accounting for the value $Re_f = 18$ marking the lower boundary of the hysteresis window and which would presumably be determined by loss of equilibrium for the locomoting state.

7. Discussion and conclusions

This study extends the QSM framework for intermediate-Re aerodynamics to account for the emergent flight dynamics of a thin plate undergoing vertical heaving oscillations in a fluid. This idealised setting serves as a testbed that allows for comparison with previous results from experiments (Vandenberghe *et al.* 2004; Ramananarivo *et al.* 2016) and direct numerical simulations (Alben & Shelley 2005; Lu & Liao 2006), and for which the behaviour is governed by relatively few dimensionless parameters, namely the mass M, flapping amplitude A, and flapping Reynolds number Re_f. By formulating aerodynamic coefficients to include appropriate dependencies on the Reynolds number Re and attack angle α, we show that the model reproduces the hallmarks of flapping-based propulsion. In particular, it captures the well-known transition from a stationary state to forward locomotion that occurs as a spontaneous symmetry breaking at a critical value of Re_f^* (Vandenberghe *et al.* 2004; Alben & Shelley 2005). Associated subtleties such as hysteresis and bistability are also reproduced. Additionally, for sufficiently large Re_f, the system robustly converges to a nearly constant Strouhal number and hence the flight speed is proportional to the flapping speed. Moreover, the attained value of $St^* = 0.2$ is consistent with previous experimental and computational studies and generally with the flapping propulsion of a wide array of aerial and aquatic organisms (Taylor *et al.* 2003; Nudds *et al.* 2004; Ramananarivo *et al.* 2016). Our model also furnishes predictions for the time scale τ' associated with reaching a terminal flight state and contributes the scaling relation $\tau'^* \sim M/A$ for sufficiently large Re_f.

Our model employs nine constant parameters, the nominal values of which we have suggested by appealing to previous studies of the aerodynamic forces on thin plates in steady flow (Ehrenstein & Eloy 2013; Ananda *et al.* 2015; Bhati *et al.* 2018; Gutierrez-Castillo *et al.* 2021; Li *et al.* 2022). The general phenomena and scaling trends are robust without any particular tuning of the parameters, while the numerical values of output quantities show different degrees of sensitivity. Our characterisations focus on the three main dynamical outputs: the transitional Reynolds number Re_f^*, the dimensionless time scale τ'^* for sufficiently large values of Re_f, and the emergent Strouhal number St^* in the same limit. The values of Re_f^* and τ'^* depend on the aerodynamic coefficients relevant to separated flow at high attack angles, which is explained by a linear stability analysis of the stationary state. In contrast, the dynamically selected St^* is sensitive to a broader array of parameters, which is consistent with an equilibrium analysis of the forward flight state showing that the characteristic angle of attack is near the stall transition for which the full slate of aerodynamic coefficients are important.

Our model uses quasi-steady aerodynamics based on steady lift and drag to address dynamical flight behaviours that previous studies have linked to unsteady vortex-based mechanisms (Vandenberghe *et al.* 2004; Alben & Shelley 2005). For example, the selected St^* characterising steady forward flight has been connected to specific modes of vortex shedding, whereas our model sees it as a condition of force balance whose robustness reflects the relative invariance of the lift and drag coefficients across $Re = 10^2$ to 10^5. Similarly, the take-off effect at a critical Re_f^* has been attributed to wing–vortex interactions, whereas our model frames it as an instability induced by a transition from drag- to lift-dominated aerodynamics as Re is increased. The unsteady and quasi-steady views might be reconciled by seeing their apparent differences as largely interpretative and semantic, with one emphasising the causal flows and the other the effective forces. It may be that the model gives fair account of the stroke-averaged forces, although likely not the details of their variations in time. This hypothesis should be systematically tested in future work, for example by comparing with experimental force/torque measurements or direct numerical simulations under matched conditions.

The dynamical model provided here is directly applicable to 2-D flight of a thin, rigid, and symmetric wing undergoing simple heaving. It will be useful to test the model for a broader set of flapping kinematics, such as pitching oscillations or combined pitching and heaving motions. Such work may start by inserting the force coefficients derived here into the more general model of Pomerenk & Ristroph (2025) that includes rotational dynamics. Extensions to non-slender and/or asymmetric profile shapes such as foils would require appropriate modifications to the force coefficients informed by experiments or simulations (Wang 2000; Lu & Shen 2008; Shyy *et al.* 2010; Jardin, Farcy & David 2012). Flexible structures that involve significant dynamical deformations within a stroke seem beyond the reach of such a QSM framework, and there are open questions about if and how 3-D effects might be addressed. Despite the inherent limitations of quasi-steady aerodynamic modelling, the encouraging results presented here motivate future efforts to bring additional aspects of intermediate-Re motion and locomotion under their purview.

Acknowledgements. We thank S. Childress, M. Shelley, Z. J. Wang and J. Zhang for useful discussions.

Funding. This work was supported by the U.S. National Science Foundation through the award DMS-1847955.

Declaration of interests. The authors report no conflicts of interest.

References

Alben, S. & Shelley, M. 2005 Coherent locomotion as an attracting state for a free flapping body. *Proc. Natl Acad. Sci. USA* **102** (32), 11163–11166.

Ananda, G.K., Sukumar, P.P. & Selig, M.S. 2015 Measured aerodynamic characteristics of wings at low Reynolds numbers. *Aerosp. Sci. Technol.* **42**, 392–406.

Andersen, A., Pesavento, U. & Wang, Z.J. 2005*a* Analysis of transitions between fluttering, tumbling and steady descent of falling cards. *J. Fluid Mech.* **541**, 91–104.

Andersen, A., Pesavento, U. & Wang, Z.J. 2005*b* Unsteady aerodynamics of fluttering and tumbling plates. *J. Fluid Mech.* **541**, 65–90.

Anderson, J. 2011 *EBOOK: Fundamentals of Aerodynamics (SI Units)*. McGraw hill.

Anderson, J.D. & Bowden, M.L. 2005 *Introduction to Flight*, vol. 582. McGraw-Hill Higher Education New York.

Ansari, S.A., Żbikowski, R. & Knowles, K. 2006 Aerodynamic modelling of insect-like flapping flight for micro air vehicles. *Prog. Aerosp. Sci.* **42** (2), 129–172.

BERGOU, A.J., RISTROPH, L., GUCKENHEIMER, J., COHEN, I. & WANG, Z.J. 2010 Fruit flies modulate passive wing pitching to generate in-flight turns. *Phys. Rev. Lett.* **104** (14), 148101.

BHATI, A., SAWANNI, R., KULKARNI, K. & BHARDWAJ, R. 2018 Role of skin friction drag during flow-induced reconfiguration of a flexible thin plate. *J. Fluids Struct.* **77**, 134–150.

BIRCH, J.M. & DICKINSON, M.H. 2003 The influence of wing–wake interactions on the production of aerodynamic forces in flapping flight. *J. Expl Biol.* **206** (13), 2257–2272.

DICKSON, W.B. & DICKINSON, M.H. 2004 The effect of advance ratio on the aerodynamics of revolving wings. *J. Expl Biol.* **207** (24), 4269–4281.

EHRENSTEIN, U. & ELOY, C. 2013 Skin friction on a moving wall and its implications for swimming animals. *J. Fluid Mech.* **718**, 321–346.

FISH, F., SCHREIBER, C., MOORED, K., LIU, G., DONG, H. & BART-SMITH, H. 2016 Hydrodynamic performance of aquatic flapping: efficiency of underwater flight in the manta. *Aerospace* **3** (3), 20.

GODOY-DIANA, R., AIDER, J.-L. & WESFREID, J.E. 2008 Transitions in the wake of a flapping foil. *Phys. Rev. E—Stat. Nonlinear Soft Matt. Phys.* **77** (1), 016308.

GUTIERREZ-CASTILLO, P., AGUILAR-CABELLO, J., ALCALDE-MORALES, S., PARRAS, L. & DEL PINO, C. 2021 On the lift curve slope for rectangular flat plate wings at moderate reynolds number. *J. Wind Engng Ind. Aerodyn.* **208**, 104459.

HOVER, F.S., HAUGSDAL, Ø. & TRIANTAFYLLOU, M.S. 2004 Effect of angle of attack profiles in flapping foil propulsion. *J. Fluids Struct.* **19** (1), 37–47.

HU, R. & WANG, L. 2014 Motion transitions of falling plates via quasisteady aerodynamics. *Phys. Rev. E* **90** (1), 013020.

HUANG, W., LIU, H., WANG, F., WU, J. & ZHANG, H.P. 2013 Experimetal study of a freely falling plate with an inhomogeneous mass distribution. *Phys. Rev. E* **88** (5), 053008.

JARDIN, T., FARCY, A. & DAVID, L. 2012 Three-dimensional effects in hovering flapping flight. *J. Fluid Mech.* **702**, 102–125.

JONES, A.M. & KNUDSEN, J.G. 1961 Drag coefficients at low Reynolds numbers for flow past immersed bodies. *AIChE J.* **7** (1), 20–25.

KANG, C.-K., CRANFORD, J., SRIDHAR, M.K., KODALI, D., LANDRUM, D.B. & SLEGERS, N. 2018 Experimental characterization of a butterfly in climbing flight. *AIAA J.* **56** (1), 15–24.

KLOTSA, D. 2019 As above, so below, and also in between: mesoscale active matter in fluids. *Soft Matt.* **15** (44), 8946–8950.

LI, H., GOODWILL, T., WANG, Z.J. & RISTROPH, L. 2022 Centre of mass location, flight modes, stability and dynamic modelling of gliders. *J. Fluid Mech.* **937**, A6.

LIU, H. 2005 Simulation-based biological fluid dynamics in animal locomotion. *Appl. Mech. Rev.* **58** (4), 269–282.

LU, X.-Y. & LIAO, Q. 2006 Dynamic responses of a two-dimensional flapping foil motion. *Phys. Fluids* **18** (9), 098104.

LU, Y. & SHEN, G.X. 2008 Three-dimensional flow structures and evolution of the leading-edge vortices on a flapping wing. *J. Expl Biol.* **211** (8), 1221–1230.

NAKATA, T., LIU, H. & BOMPHREY, R.J. 2015 A cfd-informed quasi-steady model of flapping-wing aerodynamics. *J. Fluid Mech.* **783**, 323–343.

NUDDS, R.L., TAYLOR, G.K. & THOMAS, A.L.R. 2004 Tuning of strouhal number for high propulsive efficiency accurately predicts how wingbeat frequency and stroke amplitude relate and scale with size and flight speed in birds. *Proc. R. Soc. Lond. B: Biol. Sci.* **271** (1552), 2071–2076.

PENNYCUICK, C.J. 1996 Wingbeat frequency of birds in steady cruising flight: new data and improved predictions. *J. Expl Biol.* **199** (7), 1613–1618.

PESAVENTO, U. 2006 *Unsteady Aerodynamics of Falling Plates*. Cornell University.

PESAVENTO, U. & WANG, Z.J. 2004 Falling paper: Navier–Stokes solutions, model of fluid forces, and center of mass elevation. *Phys. Rev. Lett.* **93** (14), 144501.

POHLY, J.A., SALMON, J.L., BLUMAN, J.E., NEDUNCHEZIAN, K. & KANG, C.-K. 2018 Quasi-steady versus Navier–Stokes solutions of flapping wing aerodynamics. *Fluids* **3** (4), 81.

POMERENK, O. & RISTROPH, L. 2025 Aerodynamic equilibria and flight stability of plates at intermediate Reynolds numbers. *J. Fluid Mech.* **1014**, A24.

RAMANANARIVO, S., FANG, F., OZA, A., ZHANG, J. & RISTROPH, L. 2016 Flow interactions lead to orderly formations of flapping wings in forward flight. *Phys. Rev. Fluids* **1** (7), 071201.

RISTROPH, L., BERGOU, A.J., GUCKENHEIMER, J., WANG, Z.J. & COHEN, I. 2011 Paddling mode of forward flight in insects. *Phys. Rev. Lett.* **106** (17), 178103.

Ristroph, L., Bergou, A.J., Ristroph, G., Coumes, K., Berman, G.J., Guckenheimer, J., Wang, Z.J. & Cohen, I. 2010 Discovering the flight autostabilizer of fruit flies by inducing aerial stumbles. *Proc. Natl Acad. Sci. USA* **107** (11), 4820–4824.

Ristroph, L., Ristroph, G., Morozova, S., Bergou, A.J., Chang, S., Guckenheimer, J., Wang, Z.J. & Cohen, I. 2013 Active and passive stabilization of body pitch in insect flight. *J. R. Soc. Interface* **10** (85), 20130237.

Sane, S.P. 2001 *The Aerodynamics of Flapping Wings*. University of California.

Sane, S.P. 2003 The aerodynamics of insect flight. *J. Expl Biol.* **206** (23), 4191–4208.

Sane, S.P. & Dickinson, M.H. 2001 The control of flight force by a flapping wing: lift and drag production. *J. Expl Biol.* **204** (15), 2607–2626.

Sane, S.P. & Dickinson, M.H. 2002 The aerodynamic effects of wing rotation and a revised quasi-steady model of flapping flight. *J. Expl Biol.* **205** (8), 1087–1096.

Schlichting, H. & Gersten, K. 2016 *Boundary Layer Theory*. Springer.

Shyy, W., Aono, H., Chimakurthi, S.K., Trizila, P., Kang, C.-K., Cesnik, C.E.S. & Liu, H. 2010 Recent progress in flapping wing aerodynamics and aeroelasticity. *Prog. Aerosp. Sci.* **46** (7), 284–327.

Spagnolie, S.E., Moret, L., Shelley, M.J. & Zhang, J. 2010 Surprising behaviors in flapping locomotion with passive pitching. *Phys. Fluids* **22** (4), 041903.

Sun, M. & Tang, J. 2002 Unsteady aerodynamic force generation by a model fruit fly wing in flapping motion. *J. Expl Biol.* **205** (1), 55–70.

Taylor, G.K., Nudds, R.L. & Thomas, A.L.R. 2003 Flying and swimming animals cruise at a Strouhal number tuned for high power efficiency. *Nature* **425** (6959), 707–711.

Tomotika, S. & Aoi, T. 1953 The steady flow of a viscous fluid past an elliptic cylinder and a flat plate at small Reynolds numbers. *Q. J. Mech. Appl. Maths* **6** (3), 290–312.

Vandenberghe, N., Childress, S. & Zhang, J. 2006 On unidirectional flight of a free flapping wing. *Phys. Fluids* **18** (1), 014102.

Vandenberghe, N., Zhang, J. & Childress, S. 2004 Symmetry breaking leads to forward flapping flight. *J. Fluid Mech.* **506**, 147–155.

Vogel, S. 2008 Modes and scaling in aquatic locomotion. *Integr. Compar. Biol.* **48** (6), 702–712.

Walker, J.A. 2002 Functional morphology and virtual models: physical constraints on the design of oscillating wings, fins, legs, and feet at intermediate Reynolds numbers. *Integr. Compar. Biol.* **42** (2), 232–242.

Wang, Q., He, K.-F., Qian, W.-Q., Zhang, T.-J., Cheng, Y.-Q. & Wu, K.-Y. 2012 Unsteady aerodynamics modeling for flight dynamics application. *Acta Mechanica Sin.* **28**, 14–23.

Wang, Z.J. 2000 Vortex shedding and frequency selection in flapping flight. *J. Fluid Mech.* **410**, 323–341.

Wang, Z.J. 2005 Dissecting insect flight. *Annu. Rev. Fluid Mech.* **37** (1), 183–210.

Wang, Z.J. 2016 Insect flight: from Newton's law to neurons. *Annu. Rev. Condens. Matter Phys.* **7** (1), 281–300.

Wang, Z.J., Birch, J.M. & Dickinson, M.H. 2004 Unsteady forces and flows in low Reynolds number hovering flight: two-dimensional computations vs robotic wing experiments. *J. Expl Biol.* **207** (3), 449–460.